

High energy product in Battenberg structured magnets

S. Bance,^{1,a)} H. Oezelt,¹ T. Schrefl,^{1,2} M. Winklhofer,³ G. Hrkac,⁴ G. Zimanyi,⁵
 O. Gutfleisch,⁶ R. F. L. Evans,⁷ R. W. Chantrell,⁷ T. Shoji,⁸ M. Yano,⁸ N. Sakuma,⁸ A. Kato,⁸
 and A. Manabe⁸

¹Department of Technology, St Pölten University of Applied Sciences, A-3100 St Pölten, Austria

²Center for Integrated Sensor Systems, Danube University Krems, 2700 Wiener Neustadt, Austria

³Department of Earth and Environmental Science, Ludwig-Maximilians-University, 80333 Munich, Germany

⁴CEMPS, Harrison Building, University of Exeter, Exeter EX4 4QF, United Kingdom

⁵Department of Physics, UC Davis, Davis, California 95616, USA

⁶Institute for Materials Science, TU Darmstadt, 64287 Darmstadt, Germany

⁷Department of Physics, University of York, Heslington, York YO10 5DD, United Kingdom

⁸Toyota Motor Corp., Toyota City 471-8572, Japan

(Received 14 August 2014; accepted 29 September 2014; published online 10 November 2014)

Multiphase nano-structured permanent magnets show a high thermal stability of remanence and a high energy product while the amount of rare-earth elements is reduced. Non-zero temperature micromagnetic simulations show that a temperature coefficient of remanence of $-0.073\%/K$ and that an energy product greater than 400 kJ/m^3 can be achieved at a temperature of 450 K in a magnet containing around 40 volume percent $\text{Fe}_{65}\text{Co}_{35}$ embedded in a hard magnetic matrix.

© 2014 AIP Publishing LLC. [<http://dx.doi.org/10.1063/1.4897645>]

Permanent magnets are essential to the operation of many modern technologies and are particularly important for their role in green technologies.¹ Current $\text{Nd}_2\text{Fe}_{14}\text{B}$ based permanent magnets are usually doped with dysprosium to improve their performance at higher operating temperatures. For example, in hybrid vehicles the operating temperature is typically around $T = 450 \text{ K}$. The market price of dysprosium peaked drastically in 2010, and it is likely that producers of permanent magnet products will continue facing tighter supplies and higher prices for rare earths in the future. Progress in processing, characterization, and simulation of rare earth permanent magnets has helped continually improve their performance. We now have a much better understanding of their microstructure, particularly the importance of the grain boundary phase and grain edge defects.

A key figure of merit is the energy product, $(BH)_{\text{max}}$. For an ideal permanent magnet with rectangular hysteresis loop, the maximum possible energy product is proportional to the saturation magnetization squared $(BH)_{\text{max}} = \mu_0 M_s^2 / 4$, provided that the coercive field, H_c , exceeds half of the remanence $H_c \geq M_r / 2$. In order to produce magnets with high energy product, using fewer rare earth elements, nano-composites containing a combination of hard and soft or semi-hard phases and new intermetallic phases are presently being pursued.²⁻⁴ The high saturation magnetization of the magnetically soft phase gives a high total remanent magnetization. Provided that exchange hardening⁵ of the soft phase leads to a sufficiently high coercive field the energy product, which grows quadratically with M_r , can be improved. Generally, a structure containing soft inclusions inside a hard matrix has been shown to produce the best results. Balamurugan and co-workers⁶ proposed different ideal microstructures for exchange-coupled composite magnets. Similarly to modern high performance magnets, grains are

separated by a non-magnetic or weakly ferromagnetic grain boundary phase, in order to avoid domain wall propagation once a reversed domain has been nucleated. Each grain itself is made of a composite material whereby soft inclusions are embedded in a hard magnetic matrix. In addition to the grain boundary phase which separates the grains magnetically,⁷ modern magnets use the concept of magnetic surface hardening^{8,9} for improved coercivity. The local anisotropy field near the surfaces of each grain is increased by partially substituting Nd with Dy in $\text{Nd}_2\text{Fe}_{14}\text{B}$ based magnets. Balasubramanian and co-workers¹⁰ discussed the high temperature performance of nano-composite films composed of Hf-Co_7 nano-particles and $\text{Fe}_{65}\text{Co}_{35}$. The authors attribute the good temperature stability of the composite films to the high Co content and the wide domain wall width of the hard phase.

In this paper, we present a micromagnetic study of one building block of an ideal nano-composite structure. Soft magnetic inclusions are embedded into a $\text{Nd}_2\text{Fe}_{14}\text{B}$ matrix. The surface of the grain is made of a “superhard” shell, a material with a higher anisotropy field than that of $\text{Nd}_2\text{Fe}_{14}\text{B}$. The super-hard outer shell is intended to suppress the nucleation of reversed domains at weak points,^{11,12} such as surface defects, weakly ferromagnetic boundary phases, or sharp corners with locally high demagnetizing fields. In particular, we will show that in nano-composite magnets the super-hard shell improves both remanence and coercivity at elevated temperatures. Fig. 1 shows the schematics of the proposed microstructure of a nano-composite high energy product permanent magnet. Since the cross section of a grain has the appearance of a Battenberg cake,¹³ we refer to the composite structure as “Battenberg magnet.” This paper presents a theoretical study of the possibilities of ideal hard-soft nanostructures. The fine-scale nanostructure together with the super-hard shell are challenging to fabricate. We will investigate the temperature stability of the magnetic properties of one building block of the structure shown in

^{a)}simon.bance@fhstp.ac.at. URL: <http://academic.bancey.com>.

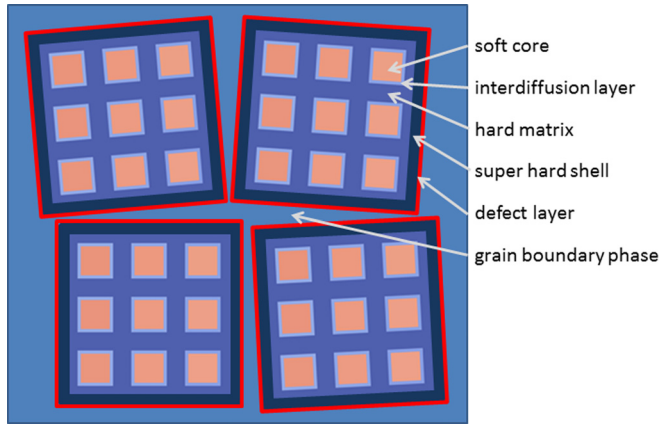


FIG. 1. Proposed microstructure of a nano-composite permanent magnet. Each grain is composed of soft magnetic inclusions embedded in a hard magnetic phase. Both phases are coupled through a thin inter-diffusion layer with properties that may be different from either of the two phases. A grain may have a super-hard shell with an anisotropy field exceeding that of the hard magnetic matrix phase. At the surface, a ferromagnetic layer with small or zero anisotropy is assumed (defect layer).

Fig. 1, whereby we compare the properties of the grain with and without a super-hard shell.

The remanent magnetization, M_r , of a composite magnet can be assumed to be proportional to the volume averaged saturation magnetization $\bar{M}_s(T) = \sum_i v_i M_{s,i}(T) / \sum_i v_i$, where v_i and $M_{s,i}(T)$ are the volume and the temperature dependent saturation magnetization of phase i , respectively. The sum is over all magnetic phases. The remanent magnetization is $M_r(T) = abc(T)\bar{M}_s(T)$, whereby the factors a , b , and $c(T)$ account for the misalignment of the grains, non-magnetic boundary phases, and the reduction of the magnetization by thermally excited spin waves, respectively. Thermal fluctuations have a two-fold effect:¹⁴ They reduce the remanent magnetization through long wave-length spin waves and they reduce the coercive field.

We apply finite element micromagnetic simulations to compute the temperature dependent hysteresis properties. The problem domain is discretized into an irregular tetrahedral finite element grid and magnetization is computed piecewise linearly. The magnetostatic interaction field is computed from the magnetic scalar potential.²³ We use a three step procedure to compute the magnetization as function of field and temperature:

- (i) The demagnetization curve is computed by minimizing the micromagnetic energy for decreasing external field with a field step of $\mu_0\Delta H = 0.01$ T. At each field, we integrate the Landau-Lifshitz equation with infinite damping²⁴ using a semi-implicit midpoint-scheme²⁵ and a modified Barzilai-Borwein step length selection.²⁶ This algorithm²⁷ resembles a gradient descent method for energy minimization. We use the temperature dependent material constants as input. Table I gives the values for the saturation magnetization, $M_s(T)$, the anisotropy constant, $K_1(T)$, and the exchange constant, $A(T)$ used in the simulations. Typically, the computed demagnetization curve shows an exchange spring behavior.^{28,29} The magnetization rotates reversibly in the soft magnetic phases

TABLE I. Intrinsic material parameters for the different magnetic phases used in the simulations. The exchange constant at 450 K was estimated from $A(T) = kM_s^2(T)$, where k is an arbitrary constant. We assume zero anisotropy in the soft magnetic $\text{Fe}_{65}\text{Co}_{35}$ phase. The magnetization values at 4.2 K are used for renormalization¹⁵ when computing the influence of thermal fluctuations on the magnetization, $M'(H, T)$.

| Name | T (K) | K_1 (MJ/m ³) | $\mu_0 M_s$ (T) | A (pJ/m) |
|---------------------------------------|---------|----------------------------|-----------------|---------------|
| $\text{Nd}_2\text{Fe}_{14}\text{B}$ | 4.2 | ... | 1.84 (Ref. 16) | ... |
| $\text{Nd}_2\text{Fe}_{14}\text{B}$ | 300 | 4.3 (Ref. 16) | 1.61 (Ref. 16) | 7.7 (Ref. 17) |
| $\text{Nd}_2\text{Fe}_{14}\text{B}$ | 450 | 2.09 (Ref. 16) | 1.29 (Ref. 16) | 4.89 |
| $\text{Sm}_2\text{Fe}_{17}\text{N}_3$ | 4.2 | ... | 1.65 (Ref. 18) | ... |
| $\text{Sm}_2\text{Fe}_{17}\text{N}_3$ | 300 | 8.6 (Ref. 19) | 1.54 (Ref. 19) | 12 (Ref. 19) |
| $\text{Sm}_2\text{Fe}_{17}\text{N}_3$ | 450 | 4.78 (Ref. 20) | 1.37 (Ref. 20) | 9.5 |
| $\text{Fe}_{65}\text{Co}_{35}$ | 4.2 | ... | 2.45 (Ref. 21) | ... |
| $\text{Fe}_{65}\text{Co}_{35}$ | 300 | 0 | 2.45 (Ref. 19) | 35 (Ref. 22) |
| $\text{Fe}_{65}\text{Co}_{35}$ | 450 | 0 | 2.39 (Ref. 21) | 33.4 |

before irreversible switching occurs. This initial computed demagnetization curve does not take thermal fluctuations into account.

- (ii) Thermally induced spin waves reduce $M(H)$ along the reversible part of the demagnetization curve. This effect may deteriorate the loop squareness and reduce the energy product. Numerically, the thermal fluctuations of the magnetization can be computed by Langevin dynamics. Starting from the magnetization configurations computed by energy minimization, we solve the stochastic Landau-Lifshitz Gilbert equation.³⁰ We use a midpoint scheme³⁰ for time integration with a time step of 8 fs. The simulations take the experimentally obtained temperature dependent values for $M_s(T)$ and $K_1(T)$ as input. In order to account for the mesh-size dependence of the results, we apply a renormalization technique,¹⁵ which scales the magnetization that is used as input for the simulations according to the local size of the finite element mesh. The renormalization technique was derived for magnets with a cubic crystal structure. The application of this method for rare-earth transition metal alloys is an approximation which we use in order to take into account the spatial variation in the size of the tetrahedrons through the structure. A more rigorous treatment of the thermal effects would require atomistic simulations taking into account the intersublattice coupling between rare-earth and transition metals. The exchange is treated micromagnetically¹⁵ using the exchange constants listed in Table I. We use the magnetization configuration $M(H)$ obtained from classical micromagnetics as input for the Langevin simulations, which give the magnetization as function of field and temperature. The new curve, $M'(H, T) < M(H)$, includes the effect of thermal fluctuations on the magnetization. This method also gives the remanence, $\mu_0 M_r(T) = B_r(T)$, as function of temperature.
- (iii) Thermal fluctuations help the system to overcome energy barriers and thus reduce the coercive field. Applying an external field changes the energy landscape. With increasing opposing field, the energy

barrier that separates the current state from the reversed state becomes smaller. Switching occurs when the barrier vanishes and the system can relax to the next deeper energy minimum.³¹ With thermal activation, the system can hop over a finite energy barrier, which leads to a reduction in the switching field. We apply the modified string method,³² in order to compute the minimum energy path from the current magnetization state to the reversed state. The magnetization configurations along the path are described by images. Each image is a replica of the total system. The minimum energy path over a saddle point is found iteratively. A single iteration step consists of two moves: First each image is relaxed by applying a few steps of the energy minimization algorithm described in (i), then the images are moved along the path so that the distance between the images is constant. We use an energy weighted distance,³³ so that there are more images next to the saddle point. We track the saddle point as a function of the applied field. The critical field value at which the energy barrier becomes $25 k_B T$ is the temperature dependent coercive field, $H_c(T)$.³⁴

Applying methods (i), (ii), and (iii) gives the temperature corrected demagnetization curve. We compare the magnetic properties of a nano-structured $\text{Fe}_{65}\text{Co}_{35}/\text{Nd}_2\text{Fe}_{14}\text{B}$ grain with a $\text{Sm}_2\text{Fe}_{17}\text{N}_3$ shell and of the same structure with $\text{Sm}_2\text{Fe}_{17}\text{N}_3$ replaced by $\text{Nd}_2\text{Fe}_{14}\text{B}$. The details of the system are as follows: The grain is a cube with an edge length of 84 nm. The core of the grain is a $\text{Nd}_2\text{Fe}_{14}\text{B}$ matrix with 27 soft inclusions of cubic shape. Following a line from the center of the grain towards its surface, we see the phases as shown in Table II. The volume fraction of the soft magnetic phase is 0.42 (including the inter-diffusion layer), the volume fraction of the $\text{Nd}_2\text{Fe}_{14}\text{B}$ matrix phase is 0.3, and the volume fraction of the hard $\text{Sm}_2\text{Fe}_{17}\text{N}_3$ shell excluding the outer defect layer is 0.14. The grain is meshed into tetrahedral elements with a mesh size of 1.2 nm along the edges of the soft inclusion, which is smaller than the exchange length in $\text{Nd}_2\text{Fe}_{14}\text{B}$. Thus, the mesh size requirements for numerical micromagnetics of magnetization reversal in hard magnets is fulfilled.³⁵

First, we compute the remanence of a single phase $\text{Nd}_2\text{Fe}_{14}\text{B}$ grain at 300 K and 450 K. The resulting

TABLE II. Dimensions and materials of a single grain of the nanocomposite magnet. Materials are listed in the table as seen if following a line from the center of the cubic grain towards its surface.

| Phase | Thickness (nm) | Properties (K_1 , M_s , A) |
|-----------------|----------------|--|
| Soft phase | 9.5 | $\text{Fe}_{65}\text{Co}_{35}$ |
| Diffusion layer | 1 | $0, \sqrt{0.4}M_{s,\text{FeCo}}, 0.4A_{\text{FeCo}}$ |
| Matrix phase | 4.25 | $\text{Nd}_2\text{Fe}_{14}\text{B}$ |
| Diffusion layer | 1 | $0, \sqrt{0.4}M_{s,\text{FeCo}}, 0.4A_{\text{FeCo}}$ |
| Soft phase | 19 | $\text{Fe}_{65}\text{Co}_{35}$ |
| Diffusion layer | 1 | $0, \sqrt{0.4}M_{s,\text{FeCo}}, 0.4A_{\text{FeCo}}$ |
| Matrix phase | 2 | $\text{Nd}_2\text{Fe}_{14}\text{B}$ |
| Hard shell | 2.25 | $\text{Sm}_2\text{Fe}_{17}\text{N}_3$ |
| Defect layer | 2 | $\text{Sm}_2\text{Fe}_{17}\text{N}_3$ but $K_1 = 0$ |

temperature coefficient, α , is $-0.15\% \text{ K}^{-1}$, which is in good agreement with experiments.³⁶ The temperature coefficient for the $\text{Fe}_{65}\text{Co}_{35}/\text{Nd}_2\text{Fe}_{14}\text{B}$ grain is $-0.098\% \text{ K}^{-1}$. The improvement has to be attributed to the high saturation magnetization of the soft phase. In the system with the $\text{Sm}_2\text{Fe}_{17}\text{N}_3$ shell, α is $-0.073\% \text{ K}^{-1}$. The additional improvement is due to the better thermal stability of $\text{Sm}_2\text{Fe}_{17}\text{N}_3$ as compared to $\text{Nd}_2\text{Fe}_{14}\text{B}$: First, at 450 K the saturation magnetization of $\text{Sm}_2\text{Fe}_{17}\text{N}_3$ is higher than that of $\text{Nd}_2\text{Fe}_{14}\text{B}$ and second, the effect of thermal spin waves is less pronounced in $\text{Sm}_2\text{Fe}_{17}\text{N}_3$ owing to its higher anisotropy. The computed magnetic properties of both systems are summarized in Table III.

Fig. 2 (left) shows the energy barrier as a function of the applied field. The dashed line is a fit of the computed values of the energy barrier (hollow diamonds) to the equation $E_B(H_{\text{ext}}) = E_0(1 - H_{\text{ext}}/H_c)^n$, where n is an exponent found during fitting, for the system without the super-hard shell. The solid line gives the fit of the energy barrier data (filled circles) for the grain with the $\text{Sm}_2\text{Fe}_{17}\text{N}_3$ shell. The super-hard shell slightly improves the thermal stability resulting in larger energy barriers for each field value. The particle switches at the critical value of the external field, which is given by the intersection of $E_B(H_{\text{ext}})$ with the $25 k_B T$ line. The total field acting is the sum of the external field and the demagnetizing field. We deshear the loop with the macroscopic demagnetization factor of 1/3. The resulting $B(H)$ curves are shown on the right hand side of Fig. 2. The simulations that led to the plots took into account the reduction of the magnetization owing to long wave-length thermal spin waves and the reduction of coercivity by thermal crossing of the energy barrier.

The influence of the $\text{Sm}_2\text{Fe}_{17}\text{N}_3$ shell on the magnetic properties becomes more pronounced with increasing temperature. At 300 K (see Table III), the coercive field values are identical for the system with and without the super-hard shell. The remanence is slightly higher in the system without the shell ($\text{Sm}_2\text{Fe}_{17}\text{N}_3$ replaced by $\text{Nd}_2\text{Fe}_{14}\text{B}$). At 450 K, the situation becomes reversed (see Fig. 2 (right)): The system with the $\text{Sm}_2\text{Fe}_{17}\text{N}_3$ shell shows a higher remanence. The computed energy products for the single grain at 450 K are 434 kJ/m^3 for the system without the shell and 466 kJ/m^3 for the system with the $\text{Sm}_2\text{Fe}_{17}\text{N}_3$ shell. These values are slightly lower than the theoretical maximum because the $M(H)$ curves are not perfectly square. The improved energy product in the magnet with the $\text{Sm}_2\text{Fe}_{17}\text{N}_3$ shell is mostly due to the improved temperature dependence of $M_s(T)$ of $\text{Sm}_2\text{Fe}_{17}\text{N}_3$ as compared to $\text{Nd}_2\text{Fe}_{14}\text{B}$. The reduction of

TABLE III. Computed magnetic properties of one building block of the multi-phase nano-structured magnet. First two rows: no super-hard shell, last two rows: $\text{Sm}_2\text{Fe}_{17}\text{N}_3$ shell.

| Shell | T (K) | $\mu_0 M_r$ (T) ^a | $\mu_0 H_c$ (T) | $(BH)_{\text{max}}$ (kJ/m^3) ^b |
|---------------------------------------|---------|------------------------------|-----------------|--|
| ... | 300 | 1.81(7) | 1.26 | 560 |
| ... | 450 | 1.55(0) | 0.72 | 380 |
| $\text{Sm}_2\text{Fe}_{17}\text{N}_3$ | 300 | 1.79(2) | 1.26 | 538 |
| $\text{Sm}_2\text{Fe}_{17}\text{N}_3$ | 450 | 1.59(7) | 0.76 | 407 |

^aAligned single grain.

^bMisalignment of 10° , 5% nonmagnetic phases.

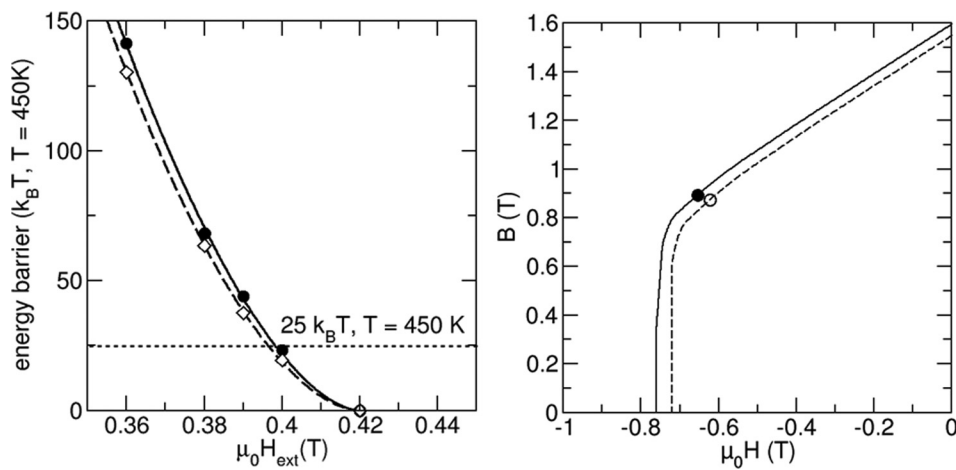


FIG. 2. Left: Data and fit of the energy barrier of a single grain as function of the applied field without the super-hard shell (hollow diamonds and dashed line) and with the super-hard shell (filled circles and solid line). Right: $B(H)$ loops for a single grain at 450 K. The circles indicate the working point where the energy product reaches its maximum. Dashed lines: $\text{Fe}_{65}\text{Co}_{35}/\text{Nd}_2\text{Fe}_{14}\text{B}$, solid lines: $\text{Fe}_{65}\text{Co}_{35}/\text{Nd}_2\text{Fe}_{14}\text{B}/\text{Sm}_2\text{Fe}_{17}\text{N}_3$.

thermal spin waves is almost similar in the two systems, which can be seen by the ratio of the saturation magnetization of the composite to remanent magnetization, which is 0.951 and 0.937 in the systems with and without the super-hard shell, respectively.

In order to estimate the energy product of a magnet being composed of the multi-phase nano-structured grains, we have to take into account the degree of alignment and the non-magnetic grain boundary phase of the magnet. We performed simulations as a function of the field angle. As expected in hard/soft exchange coupled systems, the switching field slightly increases with increasing field angle. Assuming a misalignment of 10° and a volume fraction of 5% of nonmagnetic phases gives an alignment factor of $a = 0.985$ and a volume fraction factor $b = 0.95$. The factor $c(T)$ is already taken into account by including thermal effects in the micromagnetic simulations. The above mentioned energy product of the single grain will be reduced by the factor $(ab)^2$.

In summary, we found that a super-hard shell, for example, a thin $\text{Sm}_2\text{Fe}_{17}\text{N}_3$ layer, surrounding the nano-composite structure improves the magnetic properties of exchange spring permanent magnets at elevated temperatures. At 450 K, a magnet consisting of grains where $\text{Fe}_{65}\text{Co}_{35}$ cubes are periodically embedded in a $\text{Nd}_2\text{Fe}_{14}\text{B}$ matrix reaches an energy product of 380 kJ/m^3 . Replacing the outmost 2.25 nm thick layer of $\text{Nd}_2\text{Fe}_{14}\text{B}$ by $\text{Sm}_2\text{Fe}_{17}\text{N}_3$ improves the thermal stability, which results in an energy product exceeding 400 kJ/m^3 .

This paper is based on the results obtained from the future pioneering program “Development of magnetic material technology for high-efficiency motors” commissioned by the New Energy and Industrial Technology Development Organization (NEDO).

¹O. Gutfleisch, M. A. Willard, E. Brück, C. H. Chen, S. G. Sankar, and J. P. Liu, *Adv. Mater.* **23**, 821 (2011).

²R. Skomski and J. M. D. Coey, *Phys. Rev. B* **48**, 15812 (1993).

³J. M. D. Coey, *IEEE Trans. Magn.* **47**, 4671 (2011).

⁴R. Skomski, P. Manchanda, P. Kumar, B. Balamurugan, A. Kashyap, and D. Sellmyer, *IEEE Trans. Magn.* **49**, 3215 (2013).

⁵T. Schrefl, H. Kronmüller, and J. Fidler, *J. Magn. Magn. Mater.* **127**, L273 (1993).

⁶B. Balamurugan, D. J. Sellmyer, G. C. Hadjipanayis, and R. Skomski, *Scr. Mater.* **67**, 542 (2012).

⁷H. Sepelri-Amin, T. Ohkubo, S. Nagashima, M. Yano, T. Shoji, A. Kato, T. Schrefl, and K. Hono, *Acta Mater.* **61**, 6622 (2013).

⁸M. H. Ghandehari and J. Fidler, *Mater. Lett.* **5**, 285 (1987).

⁹H. Nakamura, K. Hirato, M. Shimano, T. Minowa, and M. Honshima, *IEEE Trans. Magn.* **41**, 3844 (2005).

¹⁰B. Balasubramanian, P. Mukherjee, R. Skomski, P. Manchanda, B. Das, and D. J. Sellmyer, *Sci. Rep.* **4**, 6265 (2014).

¹¹G. Hrkac, T. Woodcock, C. Freeman, A. Goncharov, J. Dean, T. Schrefl, and O. Gutfleisch, *Appl. Phys. Lett.* **97**, 232511 (2010).

¹²S. Bance, H. Oezelt, T. Schrefl, G. Ciuta, N. M. Dempsey, D. Givord, M. Winklhofer, G. Hrkac, G. Zimanyi, O. Gutfleisch, T. G. Woodcock, T. Shoji, M. Yano, A. Kato, and A. Manabe, *Appl. Phys. Lett.* **104**, 182408 (2014).

¹³B. V. Niekerk, *British Baking—Old Time Favorites* (Brenda Van Niekerk, 2012).

¹⁴R. Skomski, P. Kumar, G. C. Hadjipanayis, and D. J. Sellmyer, *IEEE Trans. Magn.* **49**, 3229 (2013).

¹⁵M. Kirschnner, T. Schrefl, F. Dorfbauer, G. Hrkac, D. Suess, and J. Fidler, *J. Appl. Phys.* **97**, 10E301 (2005).

¹⁶S. Hock, “Züchtung und magnetische Eigenschaften von $(\text{Fe,Al})_{14}(\text{Nd,Dy})_2\text{B}$ -Einkristallen,” Ph.D. thesis (Universität Stuttgart, 1988).

¹⁷K. Durst and H. Kronmüller, *J. Magn. Magn. Mater.* **59**, 86 (1986).

¹⁸O. Isnard, S. Miraglia, M. Guillot, and D. Fruchart, *J. Appl. Phys.* **75**, 5988 (1994).

¹⁹J. Coey, *Magnetism and Magnetic Materials* (Cambridge University Press, Cambridge, 2010).

²⁰K. Müller and D. Eckert, *IEEE Trans. Magn.* **30**, 586 (1994).

²¹K. Kawahara, D. Iemura, S. Tsurekawa, and T. Watanabe, *Mater. Trans.* **44**, 2570 (2003).

²²C. Mathieu, H.-J. Liu, K. S. Buchanan, and V. R. Inturi, *J. Appl. Phys.* **111**, 07A306 (2012).

²³C. Abert, L. Exl, G. Selke, A. Drews, and T. Schrefl, *J. Magn. Magn. Mater.* **326**, 176 (2013).

²⁴M. E. Schabes and H. N. Bertram, *J. Appl. Phys.* **64**, 1347 (1988).

²⁵C. Serpico, I. D. Mayergoyz, and G. Bertotti, *J. Appl. Phys.* **89**, 6991 (2001).

²⁶I. Loris, M. Bertero, C. D. Mol, R. Zanella, and L. Zanni, *Appl. Comput. Harmonic Anal.* **27**, 247 (2009).

²⁷L. Exl, S. Bance, F. Reichel, T. Schrefl, H. Peter Stimming, and N. J. Mauser, *J. Appl. Phys.* **115**, 17D118 (2014).

²⁸E. Kneller and R. Hawig, *IEEE Trans. Magn.* **27**, 3588 (1991).

²⁹E. Fullerton, J. Jiang, and S. Bader, *J. Magn. Magn. Mater.* **200**, 392 (1999).

³⁰V. D. Tsiantos, T. Schrefl, W. Scholz, and J. Fidler, *J. Appl. Phys.* **93**, 8576 (2003).

³¹M. Schabes, *J. Magn. Magn. Mater.* **95**, 249 (1991).

³²E. Weinan, W. Ren, and E. Vanden-Eijnden, *J. Chem. Phys.* **126**, 164103 (2007).

³³E. Plan, “Parametrization and modifications for the string method,” Ph.D. thesis (National University of Singapore, 2013).

³⁴R. Dittrich, T. Schrefl, D. Suess, W. Scholz, H. Forster, and J. Fidler, *J. Magn. Magn. Mater.* **250**, 12 (2002).

³⁵W. Rave, K. Ramstöck, and A. Hubert, *J. Magn. Magn. Mater.* **183**, 329 (1998).

³⁶M.-D. Calin and E. Helerea, in *2011 7th International Symposium on Advanced Topics in Electrical Engineering (ATEE)* (2011), pp. 1–6.